Electronic Supplementary Material (ESI) for Sustainable Energy & Fuels.

3D-Porous Electrocatalytic Foam Based on Pt@N-Doped Graphene for High Performance and Durable Polymer Electrolyte Membrane Fuel Cells.

Karthikeyan K Karuppanan,[a] Appu V Raghu,[a] Manoj Kumar Panthalingal,[b] Vijayaraghavan Thiruvenkatam,[a] Karthikeyan P[c] and Biji Pullithadathil*[a,d]

SUPPORTING INFORMATION

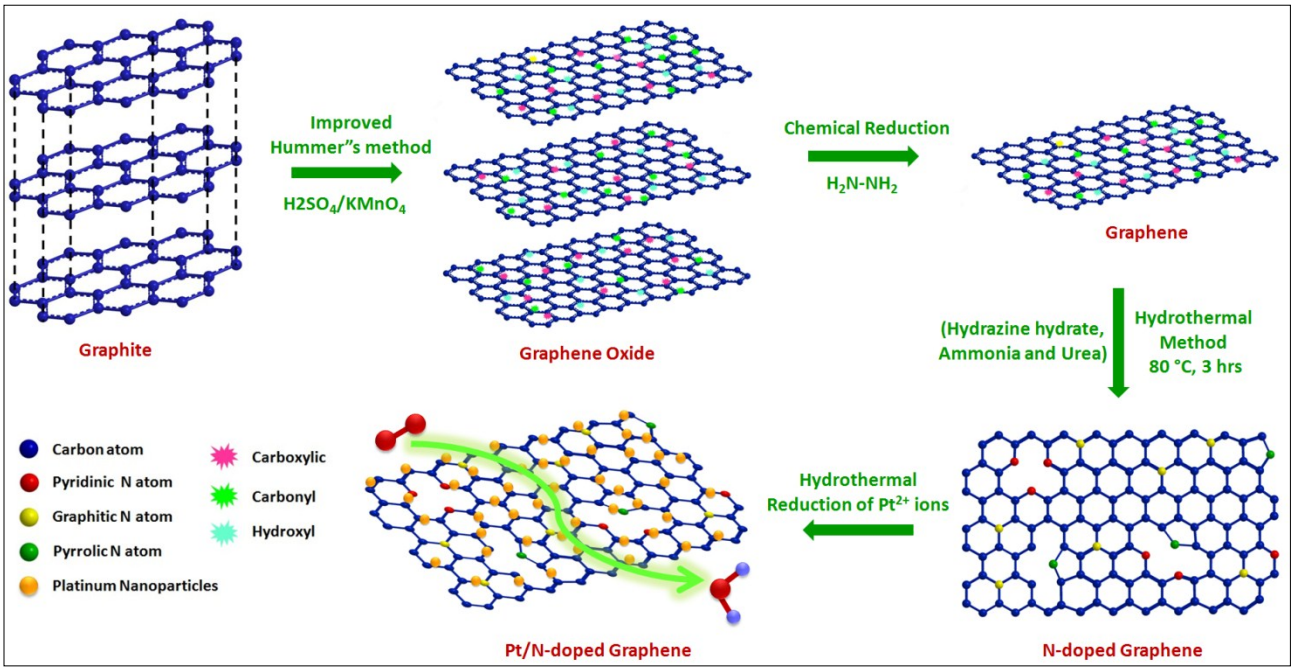

Scheme S1. Schematic illustration for preparation of Pt/N-Graphene with different N states for oxygen reduction reaction

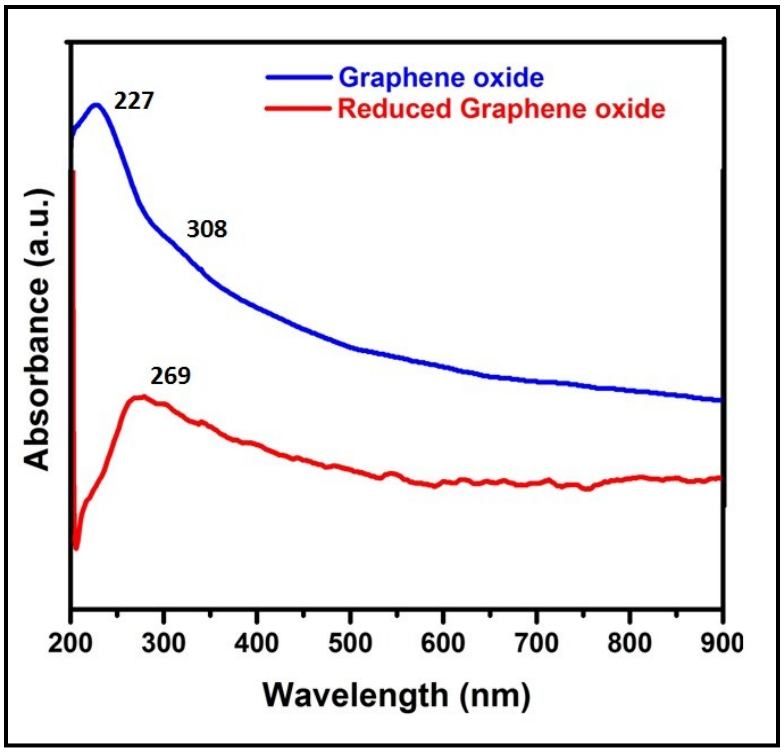

Figure S2. UV-Vis spectra of Graphene oxide and reduced Graphene oxide dispersed in ethanol.

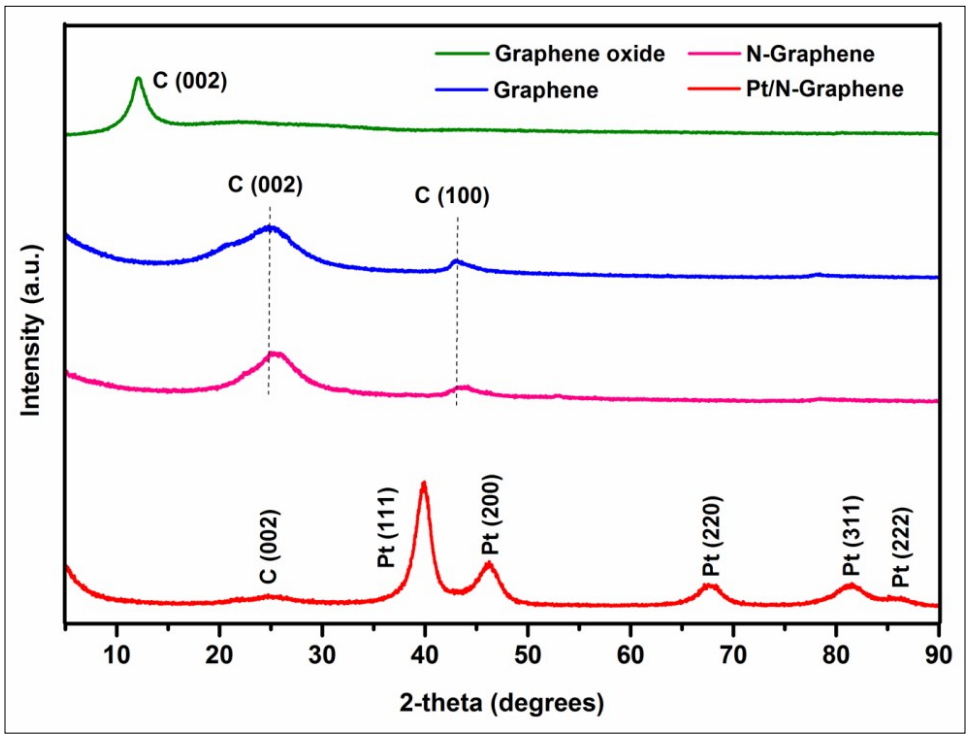

Figure S3. X-ray diffractograms of GO, Graphene, N- Graphene, 3D-Pt@N-Graphene.

The structural changes occurred during chemical processing of graphite to graphene oxide, reduced graphene oxide and nitrogen doped graphene were further supported by Raman spectral analysis (Figure S4). Figure S4 shows the spectral bands of graphene oxide emerged at 1350 and 1610 cm^{-1} for D and G band, respectively. The D band is notorious for structural distortion which is caused by the presence of edges and defects in the sp^2 carbon framework of graphene, such as grain boundaries, heteroatom introduction, etc. In addition, the G band is related to the E_{2g} in-plane vibration of sp^2 carbon atom along the axis of hexagonal framework. The calculated integrated intensity ratio of graphene oxide is 0.73. It is observed that graphene oxide showed a blue shift in D and G band to higher wave numbers compared to graphite. As per the literature, this shift could be mainly attributed to three main reasons such as (i) overlap of G band with D'band becomes active due to the formation of defects, (ii) reduced number of graphitic layers and (iii) the presence of functional group separated the isolated double bonds in the carbon framework of graphene oxide. Similarly, the reduction of graphene oxide restores the G band at 1581 cm^{-1}, which correspond to the recovery of hexagonal structure of carbon atoms with defects. The intensity of the G band is higher than that of D band as compared to graphene oxide, whereas, reduced graphene oxide showed vice versa. Table S1 summarizes the parameters obtained from Raman analysis.

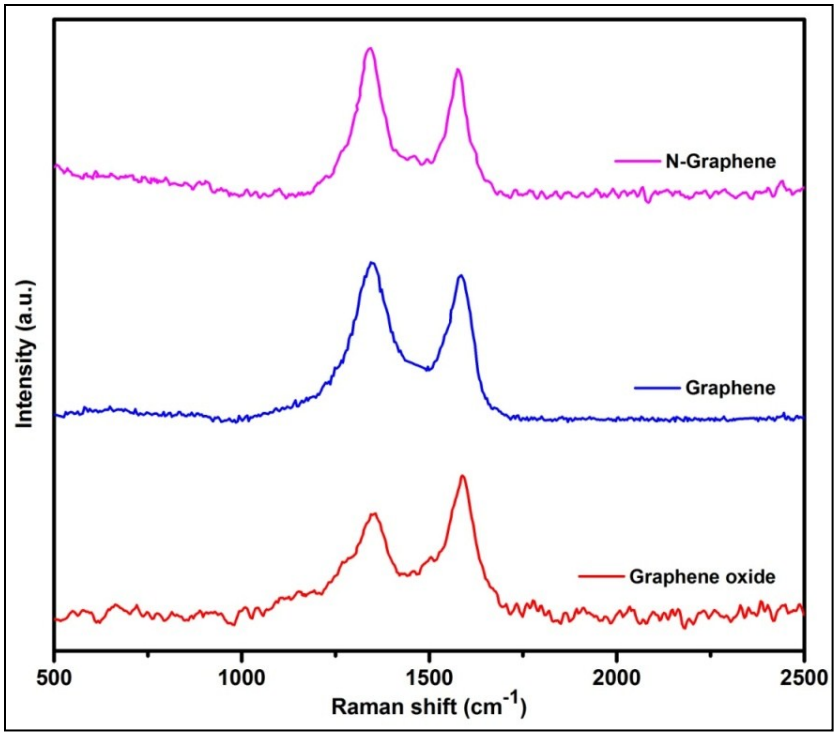

Figure S4. Raman spectra (λ= 514.5 nm) of graphene oxide, graphene and N-doped graphene.

Table S1. Raman band positions and calculated intensity ratios

Samples	D band (cm^{-1})	G band (cm^{-1})	I_D/I_G ratio
Graphene oxide	1356	1589	0.73
Graphene	1347	1585	1.09
N-Graphene	1344	1577	1.18

As shown in Figure S5, the GO showed a distinctive broad peak at 3404 cm^{-1} for O-H deformation vibration. The peaks located at 1733, 1626, 1398, 1219 and 1052 cm^{-1} could be attributed to C=O carbonyl stretching, C=C skeletal vibration, deformation vibration of C-O-C/C-OH stretching, and C-O stretching, respectively. These peaks indicate the presence of oxygen-containing functional groups such as hydroxyl, carbonyl and carboxyl which are well consistent with the reported literatures[56]. However, the absorption band intensities of graphene

were dramatically decreased after the reduction process which strongly indicated the successful exfoliation of graphene sheets and the removal of oxygen-containing functional groups. The FTIR characteristic features in graphene and N-Graphene samples were significantly different from GO. In the FTIR spectra of N-graphene, peaks appeared at ~1210 and 1550 cm^{-1} correspond to the vibrations of C-N and C=C/C=N groups respectively, which are ascribed to the replacement of carbon atoms with a nitrogen atoms. Moreover, the signals of N-Graphene are very weak as compared to GO implying the absence of oxygen-containing functional groups on the graphene sheets.

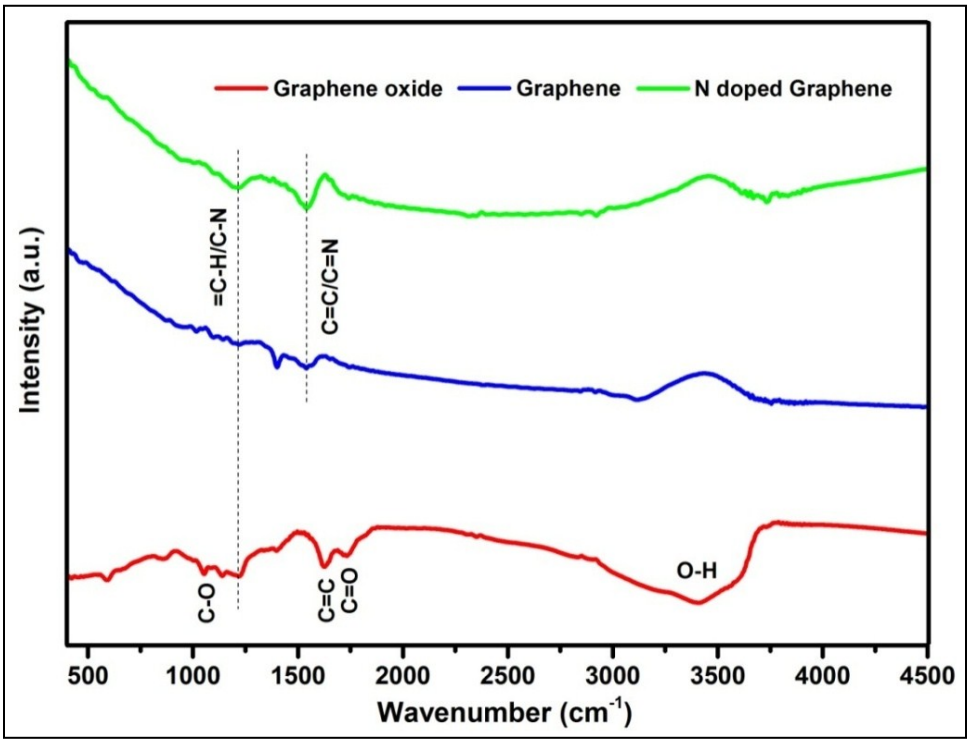

Figure S5. FTIR spectra of Graphene oxide, Graphene and nitrogen doped Graphene

Further thermogravimetric analysis (TGA) confirmed the formation of GO, graphene, N-graphene and 3D-Pt@N-Graphene foam, as shown in Figure S6. Graphene oxide was found to be thermally unstable and the first weight loss occurred even below 100 °C, which corresponds to the release of the trapped water molecules between GO sheets. The major distinctive weight

loss (~ 30 wt %) occurred at ~220 °C could be primarily attributed to pyrolytic removal of oxygen-containing functional groups yielding CO_2 and CO. Besides, small amount (~5 wt %) of weight loss was observed in these region for graphene which strongly indicates that graphene layers contain less labile oxygen functional groups. Thermal stability of the N-Graphene was greatly enhanced, indicating the presence of more proportional C-C bonds over oxygen-containing functional groups and profound reduction during nitrogen doping process. Significantly, a lesser mass change was observed for Pt incorporated N-Graphene even when the material was heated up to 1000 °C.

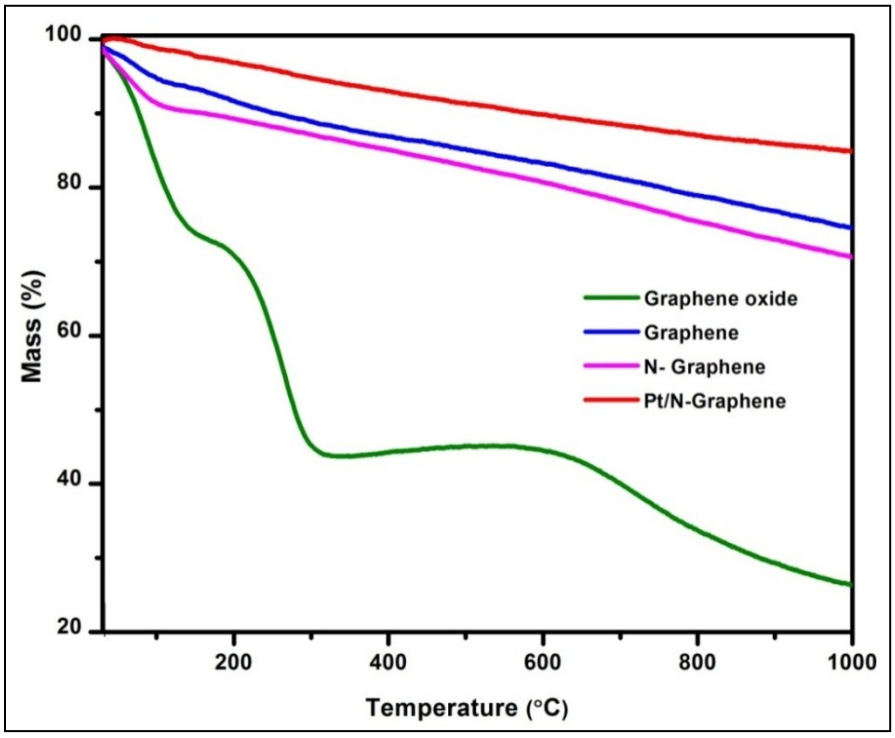

Figure S6. TGA curves of GO, Graphene, N-Graphene and Pt/N-Graphene

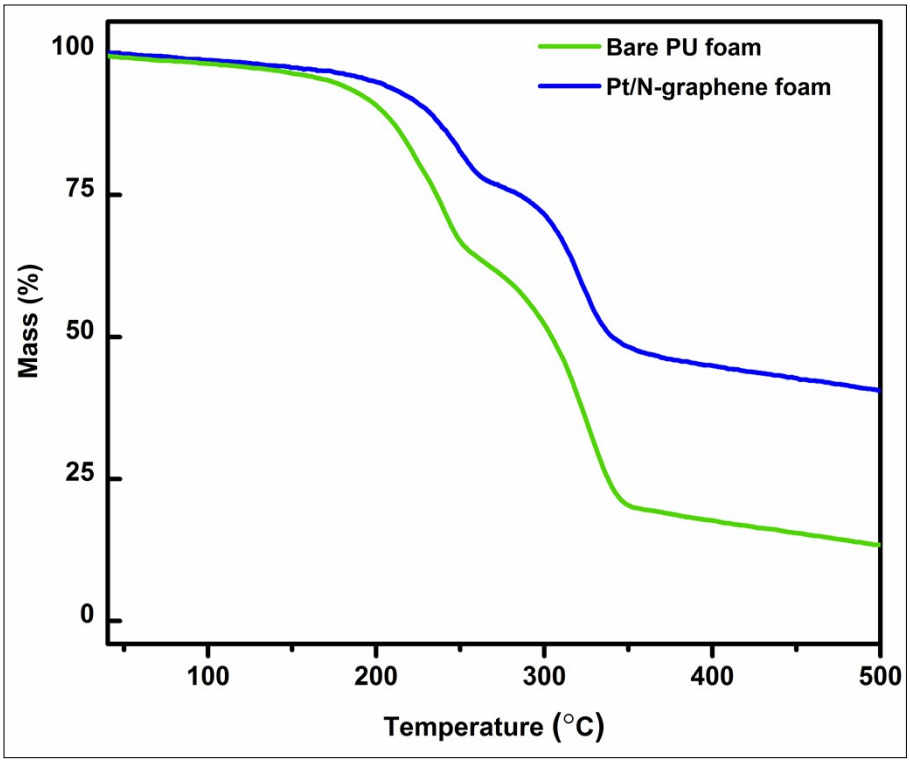

Figure S7. TGA curves of bare PU foam and 3D-Pt@N-Graphene foam

Table S2. Atomic compositions and N contributions of 3D-Pt@N-Graphene electrocatalysts obtained from XPS analysis.

Samples	Elemental composition (at %)				Nitrogen content (%)			
	C	O	N	Pt	Pyridinic-N (398.1 eV)	Pyrrolic-N (399.6 eV)	Graphitic-N (401.6 eV)	Pyridinic oxide–N (403.2 eV)
GO	62.35	37.65	-	-	-	-	-	-
Graphene	80.29	19.71	-	-	-	-	-	-
N-Graphene	80.76	12.01	7.23	-	25.13	41.68	24.92	8.27
3D-Pt@N-Graphene foam	73.68	11.34	7.17	7.81	24.64	42.71	24.81	7.84

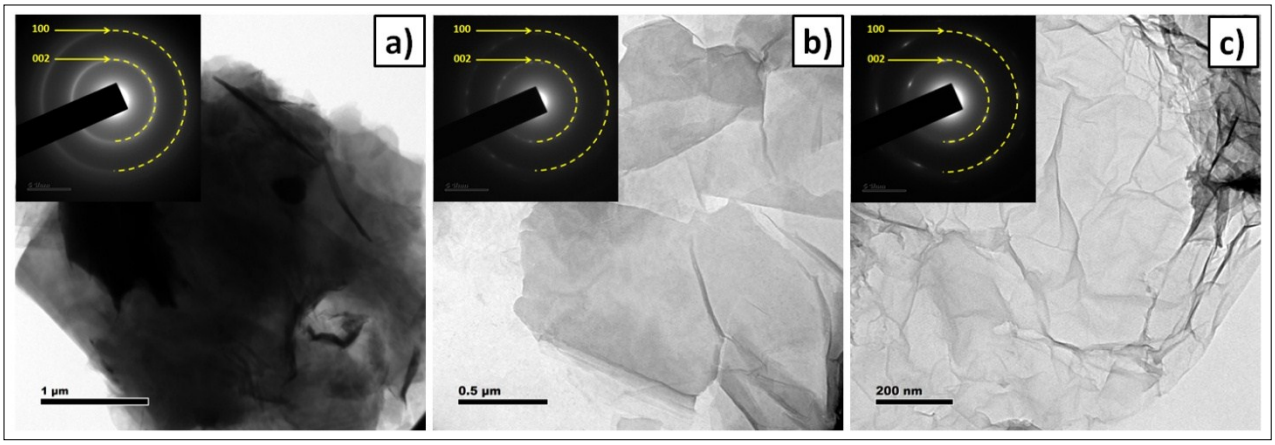

Figure S8. TEM images of pristine graphite (a), Graphene oxide (b) and Graphene (c) and their corresponding SAED patterns.

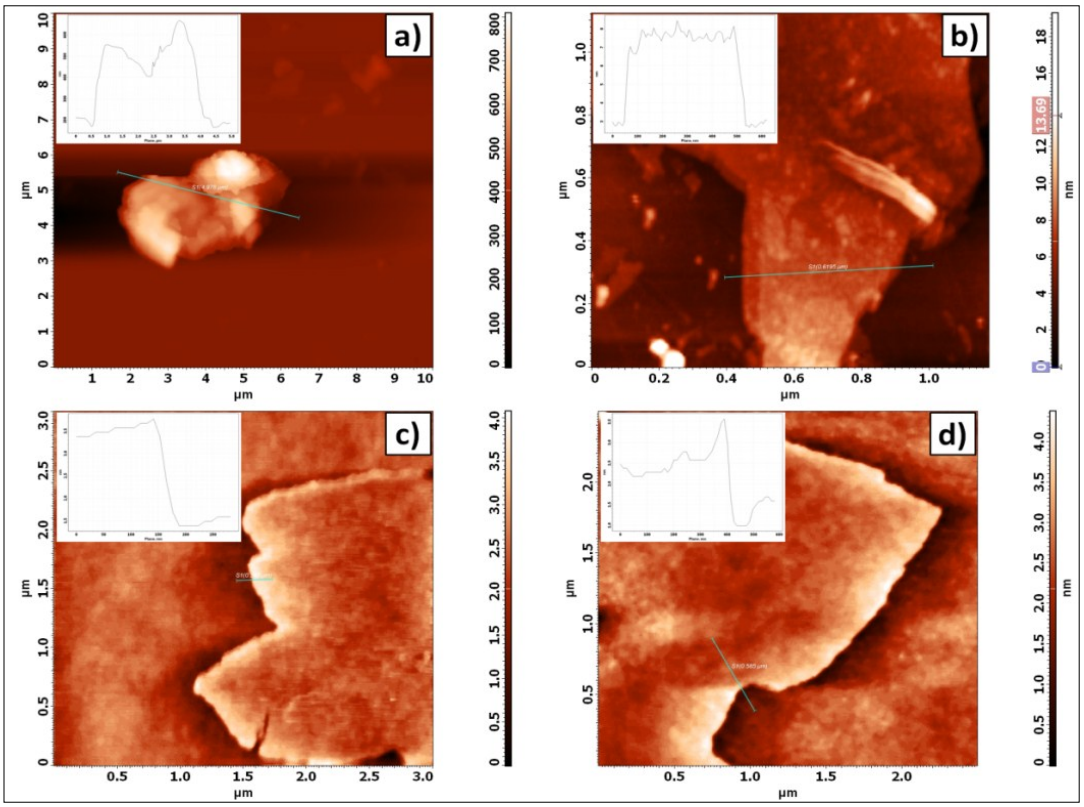

Figure S9. AFM topographic images of (a) Graphite, (b) Graphene oxide, (c) Graphene and (d) nitrogen doped Graphene (Inset: corresponding thickness analysis taken across the green line in respective images reveals a thickness).

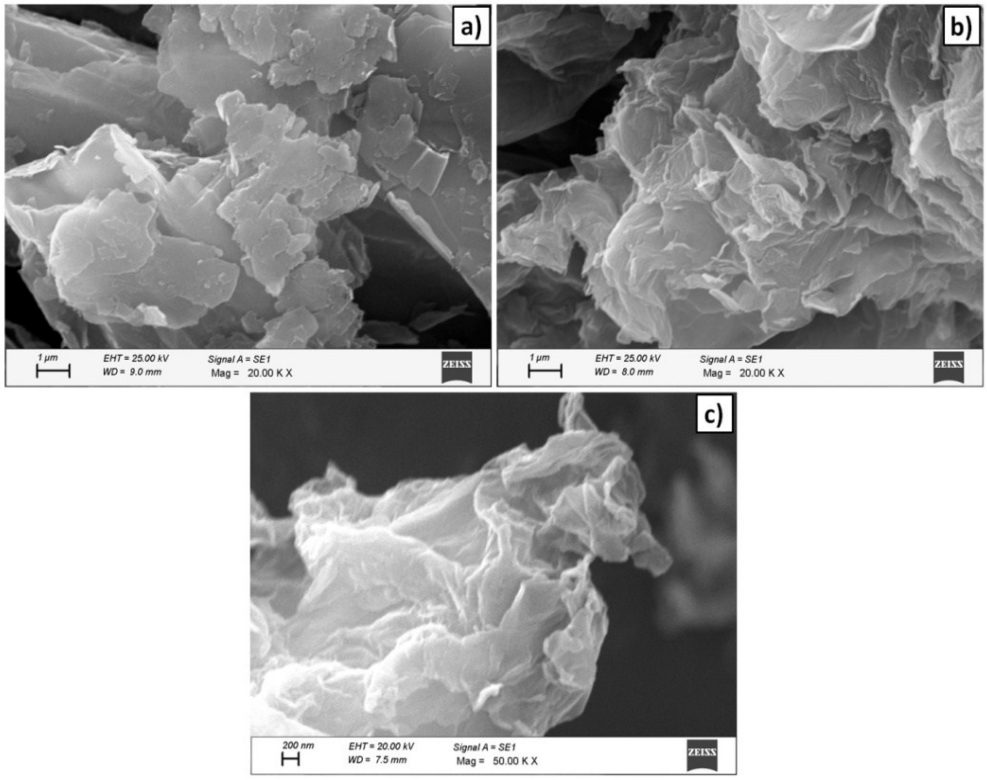

Figure S10. SEM micrographs of (a) graphite, (b) Graphene oxide and (c) Graphene.

Table S3. Textural properties of 3D-Pt@N-Graphene foam derived from BET analysis.

S_{BET} (m^2g^{-1})[a]	V_{total} (cm^3g^{-1})[b]	V_{micro}(cm^3g^{-1})[c]	V_{meso}(cm^3g^{-1})[d]	APD (nm)[e]
903	0.48	0.08	0.40	42

[a]S_{BET}- BET surface area; [b]TPV- total pore volume; [c]V_{micro}- micropore volume; [d]V_{meso}- mesopore volume; [e]APD- average pore diameter; [f] electrical conductivity

Table S4. Summary of electrochemical parameters calculated from CV of 3D-Pt@N-Graphene foam, Pt@N-Graphene and Pt/C in 0.5 M H_2SO_4.

Sample	L_{Pt} (mg)	Q (µC)	ECSA (m^2/g)

3D-Pt@N-Graphene foam	0.0194	346.0	84.9
Pt@N-Graphene	0.0192	300.9	74.6
Pt/C	0.0198	221.7	53.3

L_{Pt}, the amount of Pt loading on glassy carbon electrode; I, current density of the hydrogen desorption peak; Q, total charge; ECSA, electrochemical surface area.

Compositional and structural stability after durability test

The durability of the prepared electrocatalyst (3D-Pt@N-Graphene foam) was compared with reported electrocatalysts support materials and the present material exhibited comparatively high durability. In addition, TEM and XPS analysis was used to ensure the structural, morphological and compositional stability of the 3D-Pt@N-Graphene foam electrocatalyst after the durability testing. Figure S11(a) demonstrate that the special distribution of the Pt nanoparticles with an average size of ~2-3 nm over the graphene sheet structure with less conglomeration was retained even after the fuel cell testing and the performance was maintained Both high-resolution image and selected-area electron diffraction (SAED) (inset of Figure S11(a) analysis implies the nanocrystalline nature of Pt nanoparticles and their lattice spacing 0.225 is close to (111) plane of fcc structure of Pt, which is in consistent with the d-spacing value compared with JCPDS database (87-8646). For further insights, the high resolution Pt 4f peaks (Figure S11(b)) from XPS analysis were deconvoluted into two pairs of doublets, which are namely $4f_{5/2}$ and $4f_{7/2}$. The most intense doublet (71.6 and 74.8 eV) is due to the metallic Pt (electrochemically active species) and the second set of doublets (72.9 and 76.1 eV) could be assigned to the Pt (II) as in PtO and $Pt(OH)_2$. The calculated percentage of Pt^0 measured from the integral areas is 82.3 %

which was found to be comparatively similar to the electrocatalyst obtained before durability testing suggesting the excellent structural and compositional stability after the durability tests.

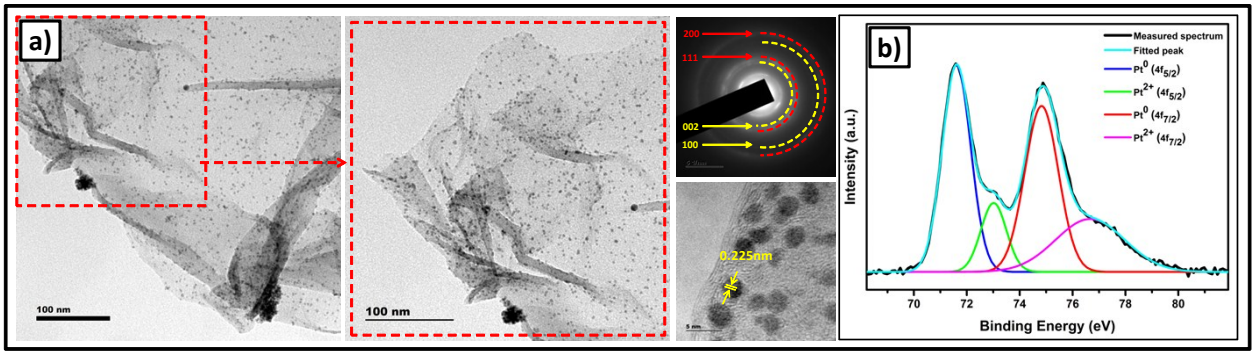

Figure S11. TEM micrographs (inset: SAED pattern and high resolution image) (a) and deconvoluted high resolution XPS Pt4f spectra (b) of 3D-Pt@N-graphene electrocatalyst after durability test.

Contact angle measurement

The hydrophilic porous surface improves loading and dispersion of active metal-related species, because a hydrophilic affinity can be created between hydrophilic pore walls and precursors, which further inhibit the random migration and agglomeration [1]. On the other hand, the hydrophilic porous surface may also influence the transport of hydrated O_2 to the electrochemically active centres under hydrated conditions, facilitating the ORR activity [2-4]. In order to illustrate the wettability features vividly, the water contact angle measurement was conducted (Dataphysics instrument, OCA 15, Germany). The time lapse visualization images of the water contact angle measurements are shown in Figure 3. Surprisingly, 3D-Pt@N-Graphene foam electrocatalyst exhibited superhydrophilic properties. Superhydrophilicity was found to form an easily wetted surface which first ensures high dispersion of metal-related active sites and

may also increase the accessibility of reactants to active centres, and thus increasing the surface and mass utilization efficiency of the catalysts.

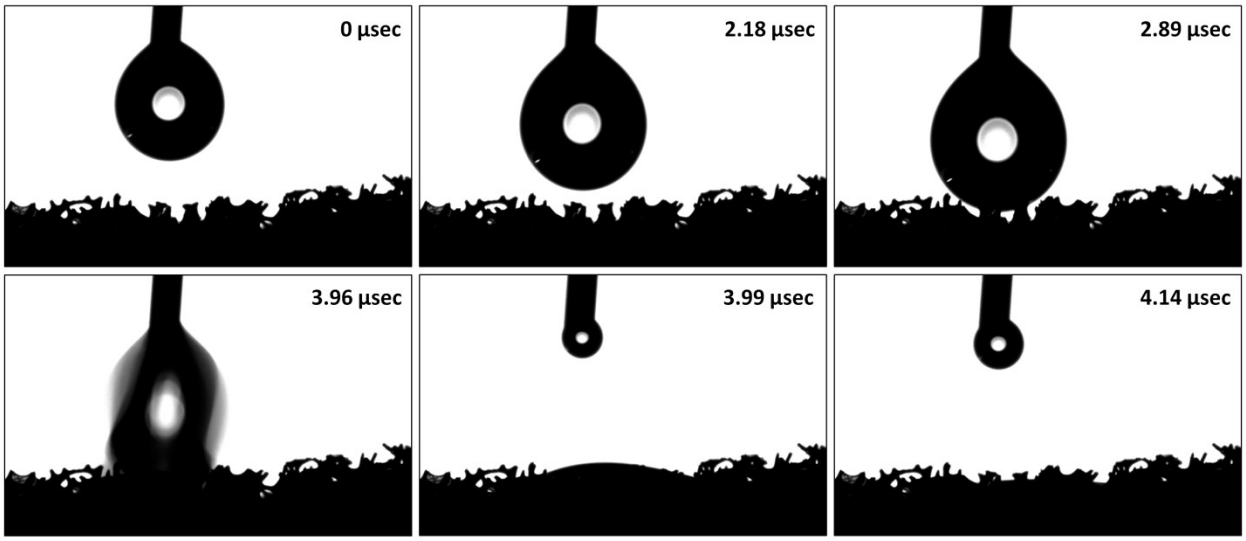

Figure S12. Time lapse visualization of water droplets on the 3D-Pt@N-Graphene foam.

References:

1 Q. Wang, Z. Zhou, Y. Lai, Y. You, J. Liu, X. Wu, E. Terefe, C. Chen, L. Song, M. Rauf, N. Tian and S. Sun, *J. Am. Chem. Soc., 2014*, **136**, 10882–10885.

2 I.-Y. Jeon, H.-J. Choi, S.-M. Jung, J.-M. Seo, M.-J. Kim, L. Dai and J.-B. Baek, *J. Am. Chem. Soc.,* 2012, **135**, 1386–1393.

3 G. P. Hao, N. R. Sahraie, Q. Zhang, S. Krause, M. Oschatz, A. Bachmatiuk, P. Strasser and S. Kaskel, *Chem. Commun*., 2015, **51**, 17285–17288.

4. Z. Lu, M. Sun, T. Xu, Y. Li, W. Xu, Z. Chang, Y. Ding, X. Sun and L. Jiang, *Adv. Mater*., 2015, **27**, 2361–2366.

Table S5. Comparison of the ORR results with the reported Pt/C electrocatalysts in various electrolytes.

Electrocatalyst	Electrolyte	Onset potential (mV)	Limiting current density mA/cm^2 (at 0.4 V)	Half wave potential (mV)	Ref.
3D-Pt@N-Graphene foam	0.5 M H_2SO_4	989	4.68 (@ 0.40 V)	895	Present work
Pt@N-Graphene	0.5 M H_2SO_4	973	4.45 (@ 0.40 V)	874	Present work
Pt/C	0.5 M H_2SO_4	936	4.09 (@ 0.40 V)	833	Present work
Other reported Pt/C catalysts	0.5 M H_2SO_4	913	~4.01 (@ 0.40 V)	770	[1]
	0.5 M H_2SO_4	750	4.00 (@ 0.46 V)	620	[2]
	0.5 M H_2SO_4	847	4.31 (@ 0.40 V)	714	[3]
	0.5 M H_2SO_4	850	~4.40 (@ 0.40 V)	749	[4]
	0.5 M H_2SO_4	900	3.98 (@ 0.30 V)	~800	[5]
	0.5 M H_2SO_4	710	2.86 (@ 0.40 V)	~820	[6]
	0.5 M H_2SO_4	915	3.1 (@ 0.70 V)	~830	[7]
	0.5 M H_2SO_4	921	3.6 (@ 0.40 V)	850	[8]
	0.5 M H_2SO_4	~750	~2.25 (@ 0.20 V)	~600	[9]
	0.5 M H_2SO_4	897	3.75 (@ 0.40 V)	706	[10]
	0.5 M H_2SO_4	910	4.39 (@ 0.30 V)	810	[11]
	0.5 M H_2SO_4	900	~3.3 (@ 0.40 V)	732	[12]
	0.5 M H_2SO_4	810	~3.1 (@ 0.40 V)	770	[13]
	0.5 M H_2SO_4	~720	~3.5 (@ 0.40 V)	~850	[14]
	0.5 M H_2SO_4	~910	~4.0 (@ 0.40 V)	~840	[15]
	0.1 M KOH	920	~4.3 (@ 0.40 V)	820	[16]

	0.1 M KOH	940	5.46 (@ 0.40 V)	830	[17]
	0.1 M KOH	~920	5.47(@ 0.40 V)	830	[18]
	0.1 M KOH	945	5.22(@ 0.40 V)	850	[19]
	0.1 M $HClO_4$	~950	5.50 (@ 0.40 V)	~860	[20]

References:

(1) Wu, N.; Wang, Y.; Lei, Y.; Wang, B.; Han, C.; Gou, Y.; Shi, Q. *Nat. Publ. Gr.* **2015**, No. November, 1–9.

(2) Ferrero, G. A.; Preuss, K.; Marinovic, A.; Jorge, A. B.; Mansor, N.; Brett, D. J. L.; Fuertes, A. B.; Sevilla, M.; Titirici, M. M. *ACS Nano* **2016**, *10* (6), 5922–5932.

(3) Wang, Y.; Jin, J.; Yang, S.; Li, G.; Qiao, J. *Electrochim. Acta* **2015**, *177*, 181–189.

(4) Lv, H.; Cheng, N.; Peng, T.; Pan, M.; Mu, S. *J. Mater. Chem.* **2012**, *22* (3), 1135–1141.

(5) Yin, J.; Qiu, Y.; Yu, J. *J. Electroanal. Chem.* **2013**, *702* (2013), 56–59.

(6) Yin, J.; Qiu, Y.; Yu, J. *Electrochem. commun.* **2013**, *30*, 1–4.

(7) Rao, C. V.; Viswanathan, B. *J. Phys. Chem. C* **2009**, *113* (43), 18907–18913.

(8) Li, Q.; Xu, P.; Zhang, B.; Wu, G.; Zhao, H.; Fu, E.; Wang, H.-L. *Nanoscale* **2013**, *5* (16), 7397.

(9) Parvez, K.; Yang, S.; Hernandez, Y.; Winter, A.; Turchanin, A.; Feng, X.; Müllen, K. *ACS Nano* **2012**, *6* (11), 9541–9550.

(10) Mohanraju, K.; Kousik, G.; Cindrella, L. *New J. Chem.* **2016**, *40* (10), 8681–8695.

(11) Jin, H.; Zhang, H.; Zhong, H.; Zhang, J. *Energy Environ. Sci.* **2011**, *4* (9), 3389.

(12) Zou, B.; Wang, X. X.; Huang, X. X.; Wang, J. N. *Chem. Commun.* **2015**, *51* (4), 741–744.

(13) Yang, L.; Kimmel, Y. C.; Lu, Q.; Chen, J. G. *J. Power Sources* **2015**, *287*, 196–202.

(14) Xiao, H.; Shao, Z. G.; Zhang, G.; Gao, Y.; Lu, W.; Yi, B. *Carbon N. Y.* **2013**, *57*, 443–451.

(15) Sun, X.; Song, P.; Chen, T.; Liu, J.; Xu, W. *Chem. Commun.* **2013**, *49* (87), 10296–10298.

(16) Lin, X. X.; Wang, A. J.; Fang, K. M.; Yuan, J.; Feng, J. J. *ACS Sustain. Chem. Eng.* **2017**, *5* (10), 8675–8683.

(17) Jiang, H.; Liu, Y.; Hao, J.; Wang, Y.; Li, W.; Li, J. *ACS Sustain. Chem. Eng.* **2017**, *5* (6), 5341–5350.

(18) Ma, X.-X.; Dai, X.-H.; He, X.-Q. *ACS Sustain. Chem. Eng.* **2017**.

(19) Zhao, H.; Weng, C.-C.; Hu, Z.-P.; Ge, L.; Yuan, Z.-Y. *ACS Sustain. Chem. Eng.* **2017**, *5* (11), 9914–9922.

(20) Coleman, E. J.; Chowdhury, M. H.; Co, A. C. ACS Catal. 2015, 5 (2), 1245–1253.